Volume 387, December 1, 2012   ISSN 0021-9797

ELSEVIER

Journal of
COLLOID AND INTERFACE SCIENCE

From Valeria Garbin, John C. Crocker, and Kathleen J. Stebe, *pages 1–11*

www.elsevier.com/locate/jcis

Mass-mobility characterization of flame-made ZrO$_2$ aerosols: Primary particle diameter and extent of aggregation

M.L. Eggersdorfer [a], A.J. Gröhn [a], C.M. Sorensen [b], P.H. McMurry [c], S.E. Pratsinis [a,*]

[a] Particle Technology Laboratory, Institute of Process Engineering, Department of Mechanical and Process Engineering, ETH Zurich, Sonneggstrasse 3, CH-8092 Zürich, Switzerland
[b] Condensed Matter Laboratory, Department of Physics, Cardwell Hall, Kansas State University, Manhattan, KS 66506-2601, USA
[c] Particle Technology Laboratory, Department of Mechanical Engineering, University of Minnesota, 111 Church Street SE, Minneapolis, MN 55455, USA

ARTICLE INFO

ABSTRACT

Gas-borne nanoparticles undergoing coagulation and sintering form irregular or fractal-like structures affecting their transport, light scattering, effective surface area, and density. Here, zirconia (ZrO$_2$) nanoparticles are generated by scalable spray combustion, and their mobility diameter and mass are obtained nearly *in situ* by differential mobility analyzer (DMA) and aerosol particle mass (APM) measurements. Using these data, the density of ZrO$_2$ and a power law between mobility and primary particle diameters, the structure of fractal-like particles is determined (mass-mobility exponent, prefactor and average number, and surface area mean diameter of primary particles, d_{va}). The d_{va} determined by DMA–APM measurements and this power law is in good agreement with the d_{va} obtained by *ex situ* nitrogen adsorption and microscopic analysis. Using this combination of measurements and above power law, the effect of flame spray process parameters (e.g., precursor solution and oxygen flow rate as well as zirconium concentration) on fractal-like particle structure characteristics is investigated in detail. This reveals that predominantly agglomerates (physically-bonded particles) and aggregates (chemically- or sinter-bonded particles) of nanoparticles are formed at low and high particle concentrations, respectively.

1. Introduction

Aerosol particles are formed by natural and man-made processes, often resulting in fractal-like particle structures. These particles can be held together by either physical forces (van der Waals or electrostatic) resulting in agglomerates or chemical forces (sinter, ionic or covalent) resulting in aggregates. It should be noted here that these definitions have been used interchangeably in the literature: one's agglomerate might be an aggregate for another. The transport and optical properties of these structures are determined mainly by the composition, number, diameter, and geometric arrangement of their constituent primary particles [1]. These properties may also affect the health impact of these particles [2] as the potential toxicity of inhaled nanoparticles correlates better to their surface area than mass [3]. Thus, real-time characterization of primary particle sizes and specific surface area of gas-borne nanoparticles is necessary for continuous monitoring of aerosol manufacturing and airborne pollutant particle concentrations.

Mostly, *ex situ* methods have been used to characterize such structures in terms of primary particle diameter and specific surface area by counting microscopic images, nitrogen adsorption, X-ray diffraction, and light scattering. Sorensen et al. [4] performed *in situ* light-scattering measurements of soot to determine the fractal dimension and primary particle radius and number per fractal-like particle. The spectral inversion, however, is still challenging for oxide particles, for example, nonabsorbent alumina. So, Xing et al. [5] carried out *in situ* light-scattering measurements of non-spherical alumina aggregates in combination with thermophoretic sampling to obtain their primary particle diameter by transmission electron microscopy (TEM) that was required for complete analysis of the scattering data. Mueller et al. [6] found by *ex situ* small angle X-ray spectroscopy (SAXS) that silica powders made in diffusion flames at high O$_2$ flow rates were converted from non-fractals (loosely packed particles) to fractal-like structures of sinter-bonded primary particles by increasing their production rate from 9 to 17 g/h. Recently, the evolution of fractal-like structures to fully compact spheres of silica has been investigated by *in situ* SAXS [7]. This method allows real-time determination of the fractal dimension D_f and primary particle size and number but requires a synchrotron and a non-trivial inversion again of the scattering data.

Park et al. [8] combined aerosol particle mass (APM) and differential mobility analyzer (DMA) measurements to obtain aggregate or agglomerate mass, mass-mobility exponent, D_{fm}, and effective density of diesel exhaust particles. The primary particle size was determined by counting electron micrographs. Recently, Wang et al. [9] utilized a DMA, a condensation particle counter (CPC), and a nanoparticle surface area monitor (NSAM) for quasi-online

* Corresponding author.
E-mail address: pratsinis@ptl.mavt.ethz.ch (S.E. Pratsinis).

Nomenclature

a	surface area, m^2
a_a	agglomerate/aggregate projected surface area, m^2
a_{va}	primary particle projected surface area, m^2
$C(d_m)$	Cunningham slip correction
c', c_1, c_2	dimensionless drag coefficient
D_α	projected area exponent, Eq. (1)
D_f	fractal dimension
D_{fm}	mass-mobility exponent, Eqs. (2) and (3)
d	diameter, m
d_g	diameter of gyration, m
d_m	mobility diameter, m
d_{va}	surface area mean primary particle diameter (also called Sauter diameter), m
e	elementary charge, C
HAB	height above burner, m
k	prefactor
Kn	Knudsen number, $Kn = 2\lambda/d_m$
L	DMA: length between exit slit and polydisperse aerosol inlet, m
m	mass, kg
N	number concentration, cm^{-3}
n	number
PP	primary particle
Q	DMA: sheath air flow rate, $l\,min^{-1}$
q	particle charge, C
r	radius, m
SSA	specific surface area, $m^2\,kg^{-1}$
v	volume, m^3
V	volume concentration, $m^3\,m^{-3}$
V_{APM}	applied APM voltage, V

V_{DMA}	applied DMA voltage, V
X	precursor flow rate, $ml\,min^{-1}$
Y	oxygen dispersion flow rate, $l\,min^{-1}$

Greek letters

α	scaling exponent Eq. (4)
η	gas viscosity, $kg\,s^{-1}\,m^{-1}$
λ	gas mean free path, m
ρ	density, $kg\,m^{-3}$
σ	standard deviation
ω	angular velocity, $radians\,s^{-1}$

Subscripts

1, 2	indices for DMA inner and outer diameter, respectively, Eq. (A3)
APM	aerosol particle mass analyzer, Eq. (2)
a	projected agglomerate/aggregate, Eq. (1)
avg	average
B	nitrogen adsorption
c	charges
fm	mass-mobility, Eq. (2)
g	geometric
in	inner
m	normalized mass-mobility, Eq. (3)
n	number
out	outer
p	primary particle
T	transmission electron microscope, Tables 1 and 2
va	surface area mean, based on d_{va}

measurement of gas-borne nanoparticles (Universal NanoParticle Analyzer, UNPA). For loose agglomerates of $D_f < 2$, they determined the primary particle size by calibrating the UNPA sensitivity to one set of primary particle sizes from electron micrographs. Although models exist to characterize agglomerates of spherical particles, up to now, the primary particle size was obtained from electron micrographs, nitrogen adsorption, or extracted by SAXS. There is still a need for real-time characterization of fractal-like aerosol particles that are typically made by coagulation and sintering.

Here, a method is presented for extraction of the average primary particle diameter of fractal-like particles from nearly *in situ* mass-mobility measurements. This diameter is one of the key characteristics of nanomaterials as it frequently determines their catalytic, sensing, superparamagnetic, plasmonic, thermal, and other properties. So, flame-made zirconia agglomerates or aggregates are characterized by DMA–APM measurements to obtain their mass, mobility diameter, mass-mobility exponent, and prefactor for different precursor and oxygen flow rates as well as zirconium precursor concentrations [10,11]. The average primary particle number, n_{va}, and surface area mean diameter, d_{va} (or specific surface area) are obtained, for the first time to our knowledge, from such data nearly *in situ* using a recent power law between agglomerate/aggregate volume, mobility, and d_{va} [12]. These d_{va} data are compared to microscopic counting of primary particle diameters as well as nitrogen adsorption measurements, and the effect of flame process parameters on product ZrO_2 particle characteristics is elucidated.

2. Experimental

2.1. Particle production

Fractal-like zirconia particles were generated by flame spray pyrolysis (FSP) [13] of solutions of two precursors, Zirconium 2-ethylhexanoate (ZrEH, 97%, Alfa Aesar), or Valirex Zr 18% Ester with Zirconium 2-ethylhexanoic acid (ZrEHA, Umicore) both dissolved in xylene (ACS reagent, Sigma Aldrich). Four to twelve ml/min of such precursor solutions at 0.05–2 M zirconium concentration were supplied with a continuous pump (MZR-2905, HNP Mikrosysteme) through the FSP burner's center capillary (inner/outer diameter 0.41/0.72 mm). Three to seven l/min of dispersion oxygen ($\geqslant$99.95%, PanGas) were delivered through the annular gap surrounding the capillary at constant pressure drop (1.7 bar). The gas flows for the supporting flamelets were 1.25 l/min CH_4 ($\geqslant$99.5%, PanGas) and 2.5 l/min O_2 and were fed through a concentric annular slit of 10 mm inner diameter and 0.3 mm width. All gas flows were controlled by mass flow controllers (Bronkhorst). The precursor solution and oxygen flow rates, X and Y, respectively, are used to characterize the flame as X/Y flame. So, a 4/5 flame refers to 4 ml/min precursor solution and 5 l/min O_2 flow rates. In general, increasing this ratio increases particle mass concentration and the high temperature particle residence time increasing primary particle size [11]. It should be noted here that in open flames like the ones studied here, reactant/gas flow rates are essential as they determine also the amount of entrained gas into the flame reactor as it has been shown by detailed computational fluid dynamics [14,15].

2.2. Particle sampling and characterization

Fig. 1 shows the experimental setup. The flame-made aerosols were sampled by a probe (inner diameter 1.1 cm) along the flame centerline at 15–30 cm height above burner (HAB) where radially well mixed conditions prevail [14]. The sample aerosol was first diluted by a factor of 10 in a water cooled, custom-made diluter with particle-free air, which was followed by a rotating disk diluter

(MD19-1E, Matter Engineering AG) with a variable dilution factor of about 20–200 to reduce the number concentration to approximately 10^6–10^7 cm^{-3}. The particles were brought to an equilibrium charge distribution by a soft X-ray neutralizer (Model 3087, TSI Inc.) and size-classified by a differential mobility analyzer (DMA, Model 3081, TSI Inc.). The aerosol sample flow rate in the DMA was 1.5 l/min, and the sheath flow rate was varied from 4 to 7 l/min. The particle mass, m, was measured with an aerosol particle mass analyzer (APM, Model APM-3600, Kanomax), which classifies particles by their mass to charge ratio. The particles move through a thin annular gap between two rotating cylindrical electrodes and experience a centrifugal and electrostatic force. If these forces are balanced, a particle moves through the gap. Otherwise, it is deposited on the APM walls. The mass is calculated from the force balance [16]: $m \cdot r_{avg}^2 \cdot \omega^2 = V_{APM} \cdot q/(\log(r_{out}/r_{in}))$, with the inner and outer radii of the annular space r_{in} = 5 cm, r_{out} = 5.2 cm, respectively, $r_{avg} = (r_{in} + r_{out})/2$ = 5.1 cm, V_{APM} is the applied voltage, ω the angular velocity and q the particle charge. The mode of the APM analyzer mass distribution of singly charged particles is used as the average agglomerate or aggregate mass [8]. Here, multiple charge effects might not be relevant as only the average mass for a given mobility diameter, d_m, is extracted (please see Appendix A.1 for an example calculation). From the density of tetragonal zirconia (ρ = 5.72 × 10^3 kg/m^3) [17], the solid agglomerate or aggregate volume v is estimated from its measured mass. The number concentration is measured after the APM analyzer with a condensation particle counter (CPC, Model 3775, TSI Inc.).

The DMA–APM system was validated with polystyrene latex spheres (diameter d_p = 100–300 nm, PSL, Duke Scientific Corporation). DMA size-classified particles were sampled also with an electrostatic precipitator (Model 3089, TSI Inc.) at 1.5 l/min and 9500 V on carbon-coated copper grids (Plano, mesh 300) for transmission electron microscopy (TEM, FEI Tecnai F30 FEG) analysis. The primary particle diameter and geometric standard deviation were calculated by manually counting over 500 primary particles per sample on the TEM images in ImageJ [18].

Zirconia particles were also collected on glass-fiber filters (Albet-Hahnemühle, GF 6, diameter 257 mm) placed in a water-cooled filter holder with a vacuum pump (Busch, SV 1025 B). The specific surface area (SSA) was determined from a five-point nitrogen adsorption isotherm at 77.3 K (Micromeritics Tristar 3000) from the particles collected on the filter. The samples were degassed in nitrogen at 150 °C for at least 1 h (Micromeritics Flow

Fig. 1. Schematic of experimental setup; HAB: height above burner, DMA: differential mobility analyzer, APM: aerosol particle mass analyzer, CPC: condensation particle counter, TEM: transmission electron microscopy, BET: nitrogen adsorption.

prep 060) before adsorption to remove water bound to their surface from air moisture.

3. Theory of fractal-like agglomerates

3.1. Structure characteristics

The average projected area a_a of fractal-like agglomerates can be related to their number of monodisperse primary particles n_p or n_{va} for polydisperse ones of surface area mean diameter (also called Sauter diameter) d_{va} by a power law [19]:

$$n_p = n_{va} = k_a \left(\frac{a_a}{a_p} \right)^{D_\alpha}, \tag{1}$$

where $a_p = a_{va} = \pi d_p^2/4 = \pi d_{va}^2/4$ is the projected area of a primary particle with diameter d_p (d_{va}) and k_a and D_α are parameters depending on collision type and agglomerate structure that are extracted from fitting Eq. (1) to numerically-generated [19,20] or experimentally-measured particle ensembles [21]. The distinction between monodisperse and polydisperse primaries is important because upon the onset of sintering primary particles grow to different sizes depending on their location within an aggregate (e.g., their coordination number). So, the fractal-like particle volume, v, to its surface area, a, ratio is used that is equivalent to the particle diameter obtained from nitrogen adsorption measurements: $d_{va} = 6v/a$. For agglomerates of initially monodisperse particles undergoing sintering by viscous flow or grain boundary diffusion and becoming aggregates, regressions to multi-particle sintering simulations result in k_a = 1.0 and D_α = 1.07 [12]. Their mobility diameter d_m is measured and related to their mass m with DMA–APM measurements by [8]:

$$m = k_{fm} \left(\frac{d_m}{d_{va}} \right)^{D_{fm}} = k_{APM}(d_m)^{D_{fm}}, \tag{2}$$

where k_{fm} and k_{APM} are constant prefactors [8]. The d_m is the mobility or hydrodynamic diameter that corresponds to the diameter of a sphere experiencing the same drag as the agglomerate or aggregate (presented in detail below). The exponent D_{fm} is referred explicitly as mass-mobility exponent and differs from the classic diameter of gyration-based, fractal dimension, D_f [1,12,22]. Eq. (2) can be written in terms of n_p or n_{va}, assuming agglomerates of monodisperse, spherical primary particles in point contact:

$$n_p = n_{va} = \frac{m}{m_{va}} = k_m \left(\frac{d_m}{d_{va}} \right)^{D_{fm}}, \tag{3}$$

where

$$k_m = k_{fm} / \left(\pi \rho d_{va}^3 / 6 \right) = k_{APM} / \left(\pi \rho d_{va}^{3-D_{fm}} / 6 \right). \tag{4}$$

For example, agglomerates of monodisperse primary particles made by diffusion-limited cluster–cluster agglomeration (DLCA) following the scaling $n_p = n_{va} = k_n (d_g/d_{va})^{D_f}$ have D_f = 1.79 ± 0.03 and k_n = 1.39 ± 0.06 [12] consistent with Meakin [1] where d_g is the diameter of gyration. The same agglomerates have D_{fm} = 2.15 ± 0.003 and $k_m = k_a$ = 1.11 ± 0.01 also in agreement with Sorensen [22]. Clearly, the difference between D_f and D_{fm} depends on the nonlinear relation between d_g and d_m [12,23].

3.2. Mobility diameter, d_m

At least, four distinct approaches have been used to describe the relationship between d_m and the number of primary particles in an agglomerate, n_p, and their diameter, d_p. First, Chan and Dahneke [24] computed the drag force on straight (agglomerate) chains of spheres in the free molecular regime by Monte Carlo (MC)
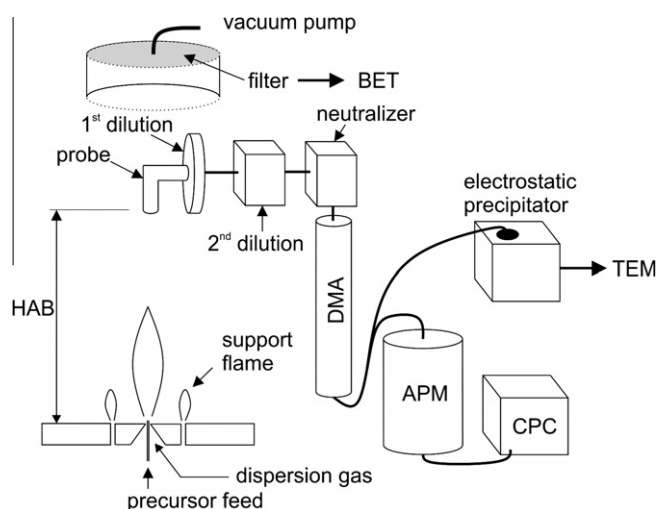
simulations with 93% of gas molecules reflecting diffusely and the rest 7% specularly from the particle surface. So, the d_m of such chains is:

$$d_m = d_p \sqrt{(n_p - 1)\frac{3c'}{\pi(8 + 0.93\pi)} + 1}, \qquad (5)$$

where $c' = 0.93c_1 + 0.07c_2$ is a dimensionless drag coefficient depending on flow field orientation. For random agglomerate orientation, $c_1 = 9.34$ for diffuse and $c_2 = 6.85$ for specular reflection, so $c' = 9.17$ [24]. Eq. (5) applies also to chains with occasional kinks and branches, as long as no significant particle screening is introduced and all primary particles are exposed [24].

Second, the d_m of an agglomerate in the free molecular [20] and transition [25] regime can be determined by its projected surface area, a_a [20], and Eq. (1):

$$d_m = 2\sqrt{\frac{a_a}{\pi}} = d_p \left(\frac{n_p}{k_a}\right)^{1/(2D_\alpha)}. \qquad (6)$$

For a Knudsen number, $Kn = \lambda/d_m$, as low as 0.28, the difference between measured d_m and Eq. (6) is only 10–20% [25], where λ is the gas mean free path. Park et al. [26] showed that the projected area (a_a) equivalent diameter, d_a, of mobility-classified diesel agglomerates nearly equals d_m, up to 220 nm, their maximum size. The d_m based on a_a of straight agglomerate chains of spheres can also be determined by [27]:

$$d_m = d_p \sqrt{1 + 0.849(n_p - 1)}. \qquad (7)$$

For the calculation of d_m, Eqs. (6) and (7) agree within 3% to Eq. (5) for chains [[25]: Eq. (7)].

Third, Lall and Friedlander [28] applied the drag force on chains [24] to open-structured agglomerates with $n_p > 12$, provided that most of primary particles are exposed for $D_f \leqslant 2$ like a straight chain. They derived a relation between n_p and d_m by equalizing the drag on chains in the free molecular regime to the Stokes drag accounting for slip correction [29], the so-called LF model here:

$$\frac{d_m}{C(d_m)} = \frac{c'n_p(d_p/2)^2}{3\pi\lambda}, \qquad (8)$$

where $C(d_m)$ is the Cunningham correction [30].

Finally, Sorensen [22] recently reviewed and analyzed the mobility of cluster–cluster agglomerates for all Kn and concluded that the d_m in the free molecular regime is best described by:

$$d_m = d_p n_p^{0.46}, \qquad (9)$$

which is identical to d_a according to Eq. (6).

3.3. Number and size of primary particles in agglomerates

The Sauter or surface area mean primary particle diameter, d_{va}, of agglomerates with volume v and surface area a is estimated with [[12]: Eq. (8)], (please see Appendix A.2 for derivation):

$$d_{va} = \frac{6v}{a} = \left(\frac{\pi k_a}{6v}(d_m)^{2D_\alpha}\right)^{1/(2D_\alpha - 3)}. \qquad (10)$$

The specific surface area (SSA) can also be obtained from d_{va}:

$$SSA = \frac{a}{m} = \frac{a}{\rho v} = \frac{6}{\rho d_{va}}. \qquad (11)$$

Here, all results are discussed with respect to d_{va} to compare it to primary particle diameters from N_2 adsorption and TEM images. Furthermore, often the SSA is required routinely for product powder specification (e.g., Aerosil 380) that is measured by N_2 adsorption. The d_{va} is an integral property of the primary particle

size distribution but gives no information about its width or shape that can be obtained by the polydispersity index or geometric standard deviation.

4. Results and discussion

4.1. Average primary particle number per agglomerate or aggregate

Here, agglomerates of 16, 64, 256, and 512 constituent monodisperse particles of $d_p = 10$ nm are generated by diffusion-limited cluster–cluster agglomeration simulations [31] with $D_f \sim 1.79$ [32]. An average over 50 agglomerates of each size is obtained. These agglomerates are sintered by viscous flow and grain boundary diffusion simulations [12], and their average number of primary particles n_{va} and resulting aggregate projected area a_a are monitored.
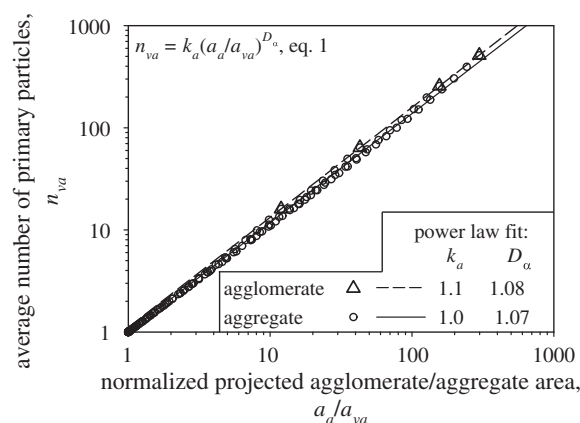
Fig. 2 shows the average number of primary particles, $n_{va} = 6v/\pi d_{va}^3$, as a function of normalized projected agglomerate/aggregate area, a_a/a_{va}. For the initial agglomerates simulated using a cluster–cluster agglomeration model (triangles), the n_{va} corresponds to the actual primary particle number n_p (here 16, 64, 256, and 512) and a_{va} to a_p in Eq. (1) as they consist of monodisperse spherical particles in point contact. When primary particles develop necks upon sintering, aggregates are formed (circles), so n_p and d_p are not well defined, so the surface area mean diameter d_{va} is used to characterize an equivalent diameter (e.g., that measured by nitrogen adsorption). The prefactor k_a and projected area exponent D_α (Eq. (1)) are determined from regression: for agglomerates (triangles)

$$k_a = 1.1 \pm 0.015 \text{ and } D_\alpha = 1.08 \pm 0.002, \qquad (12)$$

in agreement with Pierce et al. [33] while for aggregates (circles)[12]:

$$k_a = 1.0 \pm 0.04 \text{ and } D_\alpha = 1.07 \pm 0.03. \qquad (13)$$

The solid line corresponds to the relationship between n_{va} and a_a/a_{va} for aggregates undergoing sintering [12] while the broken line corresponds to agglomerates. In practical systems, primary particles have a size distribution. For agglomerates consisting of primary particles with $\sigma_g \leqslant 1.5$, the D_α obtained by regression is almost constant [[34]: Fig. 5a]. The PPs in aggregates become polydisperse during sintering and the fit of k_a and D_α for aggregates includes this effect of polydispersity. The k_a and D_α for either agglomerates or aggregates are used for polydisperse particles below to estimate d_{va}.
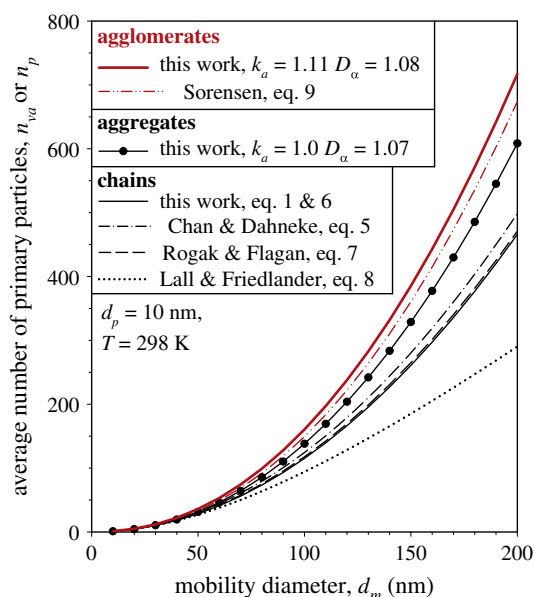

Fig. 2. The average number of primary particles, n_{va}, scales with normalized projected agglomerate/aggregate area, a_a/a_{va}, by a power law with the projected area exponent D_α and prefactor k_a. There is a tiny difference between agglomerates (spherical particles in point contact) and aggregates (partially sintered particles).

Using these values, Fig. 3 shows the predictions of the present work (Eqs. (1) and (6), solid lines) for n_{va} as a function of d_m for chains (black), aggregates (black with circles) and agglomerates (red) for D_f = 1.79 with d_p = 10 nm from the free molecular to transition regime, $Kn = 2\lambda/d_m$ = 13.34–0.67. As expected, going from chains to aggregates and to agglomerates, more primary particles (PPs) are needed to exhibit the same d_m.

For chains, the present method (solid line) is compared to Eq. (5) (dot-broken line), Eq. (7) (broken line) and Eq. (8) (dotted line). All model predictions match reasonably well for small chains ($n_p \leqslant 40$). Eq. (8), however, starts predicting systematically fewer primary particles per chain for n_p > 40 than all models. Although Lall and Friedlander [28] utilized the drag calculated by Chan and Dahneke [24] for chains, the two models (Eqs. (5) and (8)) do not match. Chan and Dahneke [24] calculated the drag force by summing over the drag of each primary particle in the chain as all primary particles are accessible for gas molecules following straight trajectories (projected area onto a plane) for D_f < 2 [20]. In the Lall and Friedlander (LF) [28] model, the Epstein drag for chains is set equal to the Stokes drag with slip correction [29] to obtain the mobility (size) of the chain agglomerate. So, the size regime of the chain defines the drag in the LF model, contrary to Chan and Dahneke [24] where the drag is determined by the size regime of the primary particles. The reasonable agreement between Chan and Dahneke (dot-broken line)[24] and Lall and Friedlander (dotted line) [28] for small agglomerates (n_p < 40) was obtained when both chain agglomerate and primary particles are essentially in the same size regime.

For agglomerates, the present primary particle number n_p (red solid line) is compared to Eq. (9) (red double-dot broken line). Both models are in good agreement as they use the average agglomerate (D_f = 1.79) collision cross section for the d_m calculation in the free molecular and transition regimes. The n_p for agglomerates (red lines) is always larger than that of chains (black lines) at the same

d_m as agglomerates consist of ramified and branched chains (Fig. 2), resulting in an aspect ratio lower than that of straight chains. The n_{va} of aggregates (solid black line with circles) lies between chains and agglomerates as the d_m of aggregates decreases during sintering while their d_{va} increases by necking [12].
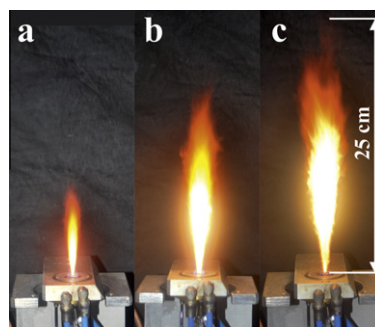
Chan and Dahneke [24] suggested that Eq. (5) is applicable for chains with occasional branches and kinks as long as no significant screening is introduced. The "sphere of influence" so-to-speak of a branch or kink extends up to a distance equal to the gas mean free path, λ, away from a primary particle surface. If such "spheres of influence" overlap, then gas molecule screening or shielding takes place. Fig. 3 shows that Eq. (5) applies best for small agglomerates. Although theoretically all PPs in agglomerates with D_f < 2 are accessible for gas molecules following straight trajectories, the collision probability depends on the PP position within the agglomerate. Realistic agglomerates have typically several branches and kinks [[35]: Figs. 3 and 4]. So, the deviation between chains and agglomerates/aggregates becomes larger with increasing d_m. Therefore, the present method (Eq. (10)) uses Eqs. (1) and (6) for the projected surface area and mobility diameter of agglomerates or aggregates to account for the additional screening by such branches. The n_{va} for agglomerates (solid red line), aggregates (solid black line with circles) and Eq. (9) (red double-dot broken line) is nearly constant factors apart. The method is applied in the following sections to flame-made zirconia (ZrO_2) agglomerates/aggregates.

4.2. Number distribution of agglomerate or aggregate mobility and primary particle diameter

Table 1 summarizes the investigated process conditions, precursor concentrations, and measured surface area mean diameters by BET, DMA–APM, and TEM.

Fig. 4 shows spray flames fed by 4(a), 8(b), and 12(c) ml/min precursor solution flow rate at 0.5 M Zr concentration and 5 l/min dispersion O_2 flow rate. The luminous flame length increases from 10.7 to 25.5 cm with increasing precursor flow rate from 4 to 12 ml/min, respectively. This increases the spray flame temperature [13] facilitating droplet evaporation, precursor conversion that enhances product particle sintering and coalescence [36].

Nine TEM images of enlarged, size-selected agglomerates with d_m = 110, 150, and 190 nm are presented in Fig. 5 for flames 4/5, 8/5, and 12/5 as described above. The maximum agglomerate dimension is typically larger than the equivalent mobility diameter because of their elongated structure. The agglomerates have open, chain-like structures consisting of several primary particles. Some primary particles have formed sinter necks, especially at the hotter flames that were created by feeding higher Zr precursor flow rates (8/5 and 12/5) and resulting in higher particle mass concentration.

Fig. 3. The relation between mobility diameter d_m and average number of primary particles n_{va} is shown for cluster–cluster-made (red lines) and straight chain (black lines) agglomerates consisting of 10 nm in diameter monodisperse primary particles and aggregates with equivalent d_m (solid black line with circles). Although agglomerates have a fractal dimension D_f = 1.79 < 2 and all primary particles are accessible by gas molecules following straight trajectories, some partial screening of interior particles by agglomerate branches is introduced. So, such agglomerates contain more primary particles than straight chains having the same mobility. The same effect is observed for aggregates, which exhibit less screening due to necking and restructuring.


Fig. 4. Increasing the precursor solution (0.5 M Zr) flow rate from 4(a) to 8(b) and 12 ml/min (c) and 5 l/min dispersion O_2 through the flame spray pyrolysis (FSP) unit increases the visible flame length and droplet/particle high temperature residence time [36].

Table 1
A summary of the investigated flame conditions and precursor concentrations with corresponding ZrO_2 production rates and measured surface area mean primary particle diameters. The error of d_{va} (Eq. (10)) corresponds to one standard deviation of d_{va} from different mobility diameters d_m, while the error of $d_{va,T}$ corresponds to the 95% confidence interval of fitting a log-normal distribution to the primary particle size distributions counted by microscopy. The flames are termed X/Y flame with X being the precursor flow rate in ml/min and Y the oxygen dispersion flow rate in l/min.

Flame condition	Precursor	Zr concentration in precursor, M (mol/l)	Production rate, g/h	$d_{va,B}$, nm	d_{va}, nm eq. 10		$d_{va,T}$, nm
					aggregate	agglomerate	
4/5	ZrEH	0.05	1.5	4.9	5.8 ± 0.08	4.8 ± 0.07	
		0.1	3.0	6.4	7.2 ± 0.6	6.0 ± 0.5	
		0.25	7.4	8.1	9.3 ± 0.6	7.7 ± 0.5	
		0.5	14.8	11.0	10.0 ± 1.3	8.3 ± 1.2	
	ZrEHA			11.3	11.3 ± 0.4	9.4 ± 0.3	10.9 ± 0.3
		1.0	29.6	12.8	12.9 ± 1.0	10.7 ± 1.5	
		2.0	59.1	14.7	13.1 ± 1.7	10.9 ± 1.6	14.1 ± 0.5
4/3		0.5	14.8	14.7	14.6 ± 0.7	12.3 ± 0.6	
4/7				9.7	10.5 ± 0.5	8.7 ± 0.4	
8/5			29.6	16.4	16.7 ± 1.4	14.1 ± 1.1	14.2 ± 0.5
12/5			44.4	24.2	24.1 ± 4.1	20.4 ± 4.0	22.3 ± 0.8
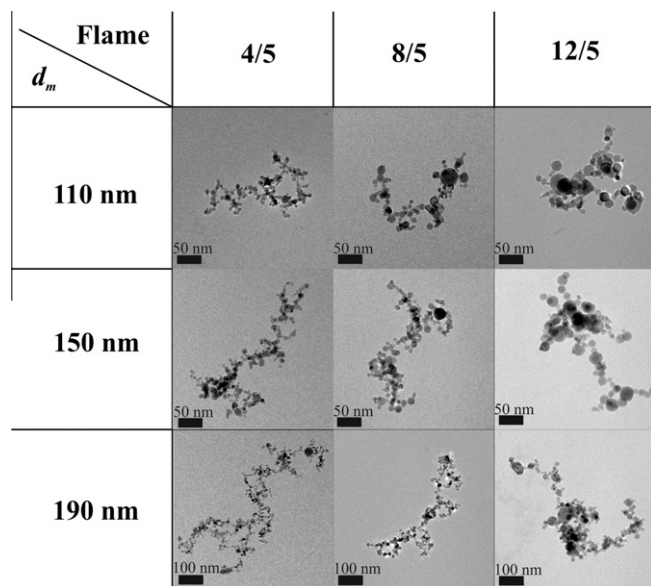
Fig. 5. TEM images of DMA size-selected agglomerates with mobility diameter d_m = 110, 150, and 190 nm generated with 4, 8, and 12 ml/min precursor flow rate (ZrEHA) at 0.5 M Zr and 5 l/min O_2 flow rate.

An increase in average primary particle size can be seen for these hotter flames also. Please note that for d_m = 190 nm, the scale bar is 100 nm to display a whole agglomerate instead of 50 nm as for the rest.

Fig. 6a shows the number distribution of ZrO_2 fractal-like particle d_m measured by a DMA at 30 cm above the FSP unit fed by 8 ml/min precursor (ZrEHA) solution at 0.5 M Zr and 5 l/min O_2 (8/5 flame). The geometric mean mobility diameter $d_{m,g}$ was 109.7 nm with a geometric standard deviation $\sigma_{m,g}$ = 1.59, indicative of fractal-like particles of $D_f \approx 2$ that have attained a self-preserving size distribution [37]. The total number concentration is $N = 1.33 \times 10^6$ #/cm³. Multiple charge correction for spheres using the Fuchs–Hoppel–Frick distribution was applied [38] (please see Appendix A.3 for the as measured size distribution). For the

estimation of d_{va} from DMA–APM measurements, however, the total number concentration and equilibrium charge distribution are not required as described above.

Fig. 6b shows the normalized primary particle size distribution of these agglomerates or aggregates by counting more than 3000 primary particles in enlarged TEM images of individual fractal-like structures. More specifically, fractal-like particles with d_m = 110, 150, and 190 nm were sampled after the DMA and more than 500 primary particle diameters were counted for each d_m. For obtaining a reliable average particle diameter and geometric standard deviation, counting 500 PPs is sufficient [39]. For example, counting more than 400 primary particles made in flame 8/5 and d_m = 110, 150, and 190 nm results an error of < 6% for the $d_{p,gT}$ and <1.5% for the $\sigma_{p,gT}$. The primary particle size distribution is described well by a log-normal distribution [40] with $d_{va,T}$ = 14.2 nm, geometric mean primary particle diameter $d_{p,gT}$ = 9.7 nm, and geometric standard deviation, $\sigma_{p,gT}$ = 1.48. This is consistent with the self-preserving size distribution (SPSD) of spherical particles by Brownian coagulation of 1.46 in the free molecular regime [[41]: Fig. 3], where particle growth mainly takes place here. The fact that σ_g has not been reduced below the theoretical values indicates that no significant necking has taken place yet [36] or that primary particles in a fractal-like particle have come from different streamlines and residence time distributions.

Table 2 summarizes the counts from electron micrographs of ZrO_2 primary particles for each d_m made at flames 4/5, 8/5 and 12/5 at 0.5 M Zr using the ZrEHA precursor. The $d_{p,gT}$, $d_{va,T}$, and $\sigma_{p,gT}$ are independent of d_m for all investigated flame conditions and so an average over all three d_m (Table 2) is shown as inset in Fig. 6b for flame 8/5. According to Table 2, both $d_{p,gT}$ and $\sigma_{p,gT}$ increase with increasing precursor solution flow rate from 8.1 to 13.4 nm and 1.37 to 1.57, respectively, consistent with Mueller et al. [10]. The increase in $d_{va,T}$ from 10.9 to 22.3 nm is even stronger as the PP distribution broadens, and this average is more sensitive to the large tail of the distribution. The 12/5 flame is the longest flame (Fig. 4, 25.5 cm, luminous zone) and has the largest $\sigma_{p,gT}$ = 1.57, due to the prolonged duration of particle formation in spray flames resulting in a broader distribution of high temperature residence times compared to the 8/5 or 4/5 flames [10].
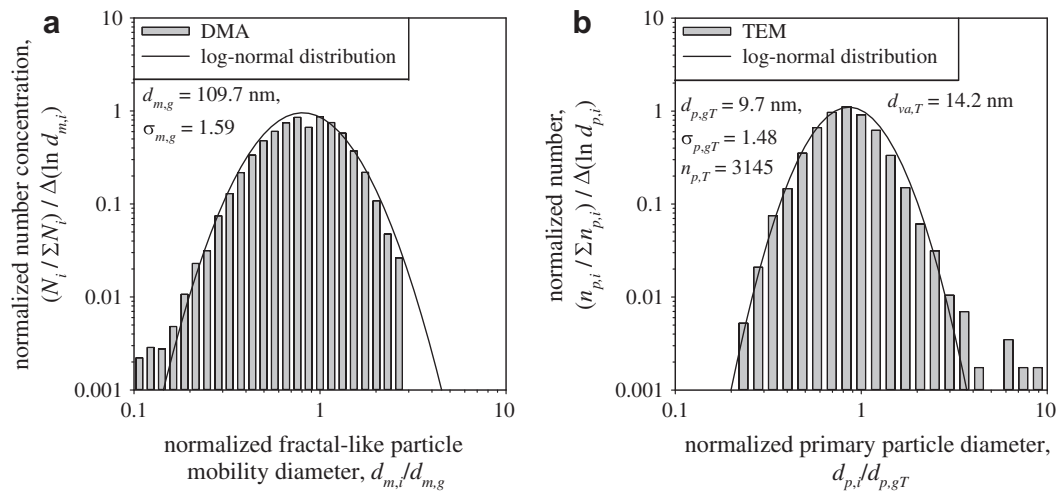
Fig. 6. (a) The mobility size distribution of fractal-like particles generated with 8 ml/min precursor and 5 l/min O_2 flow rate at 0.5 M Zr concentration have a geometric mean mobility diameter, $d_{m,g}$ = 109.7 nm with a standard deviation $\sigma_{m,g}$ = 1.59 and total number concentration $N = 1.33 \times 10^6$ #/cm^3 measured by a differential mobility analyzer (DMA). (b) The primary particle size distribution obtained by counting over 3000 primary particles in transmission electron microscope (TEM) images of fractal-like particles with d_m = 110, 150, and 190 nm. The primary particle size distributions are independent of mobility size and have a geometric mean diameter of $d_{p,gT}$ = 9.7 nm, $\sigma_{p,gT}$ = 1.48, and surface area mean diameter $d_{va,T}$ = 14.2 nm.

Table 2
Statistics of the primary particle size distribution from counting TEM images for DMA size-selected aggregates or agglomerates that were generated by FSP of 4, 8, and 12 ml/min of precursor (ZrEHA) solution at 0.5 M Zr and 5 l/min dispersion O_2 flow rate.

Flame	DMA Mobility diameter, d_m, nm	Primary Particle Diameter by Microscopic Counting						
		Surface area mean diameter, nm		Geometric				Number of counted particles
				mean diameter, nm		standard deviation		
		$d_{va,T}$	$\overline{d}_{va,T}$	$d_{p,gT}$	$\overline{d}_{p,gT}$	$\sigma_{p,gT}$	$\overline{\sigma}_{p,gT}$	
4/5	80	10.66		8.35		1.37		502
	110	10.29		8.09		1.36		576
	150	9.72	10.9	7.66	8.1	1.36	1.37	712
	190	12.09		8.78		1.43		1238
8/5	110	14.38		10.23		1.45		570
	150	14.64	14.2	9.98	9.7	1.48	1.48	1085
	190	13.63		9.27		1.48		1490
12/5	110	21.74		13.38		1.55		972
	150	21.75	22.3	13.29	13.4	1.56	1.57	1827
	190	23.24		13.61		1.59		1729

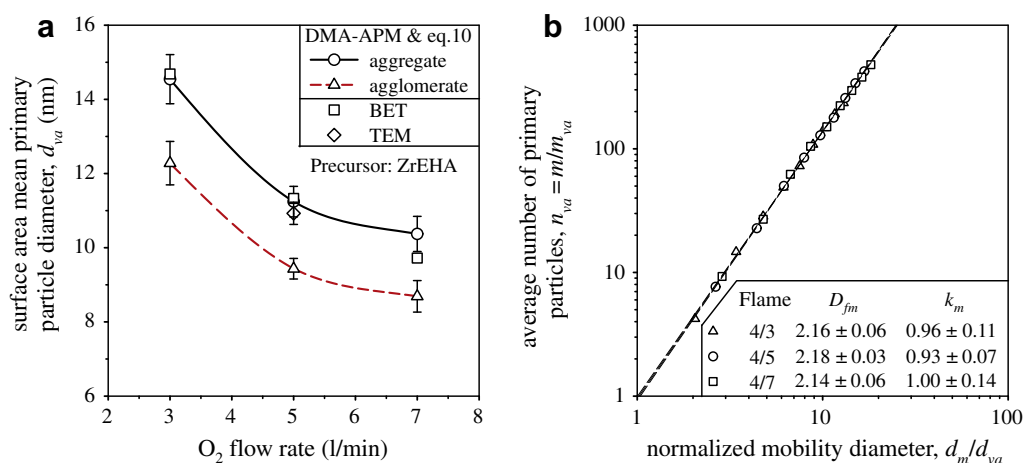### 4.3. Particle structure: mass-mobility exponent, prefactor, and primary particle size of ZrO$_2$ agglomerates

4.3.1. Effect of oxygen flow rate

Fig. 7 shows the effect of O_2 flow rate on (a) d_{va} and (b) D_{fm} and k_m for 4 ml/min ZrEHA precursor feed rate at 0.5 M Zr concentration

(Table 1). Higher O_2 flow rates result in a shorter flame, higher flow velocity, additional ambient air entrainment, and higher flame cooling rate and thus a shorter particle residence time at high temperature as well as lower ZrO$_2$ concentration reducing coagulation and sintering rates that favor smaller d_{va} [42].

So, Fig. 7a shows the d_{va} from DMA–APM analysis and Eq. (10) for agglomerates (triangles, broken red line, k_a = 1.11 and
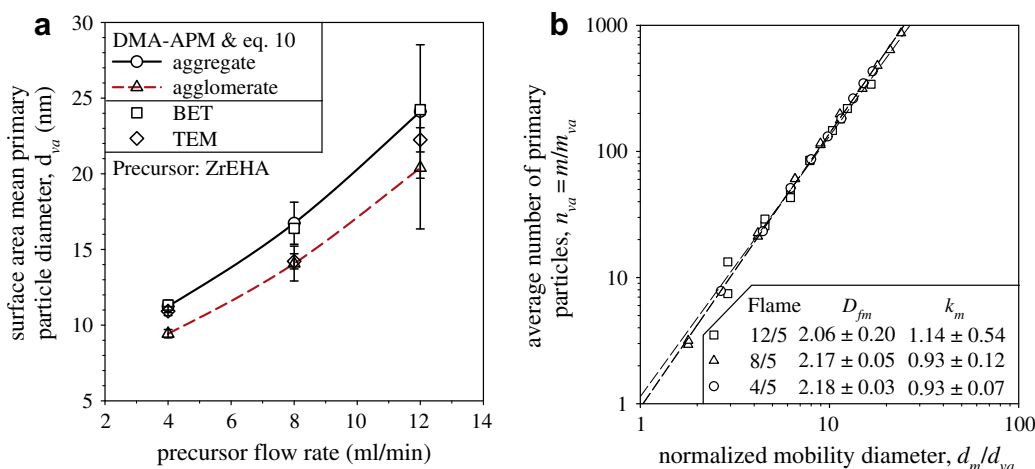
Fig. 7. The effect of O_2 flow rate on (a) surface area mean ZrO_2 primary particle diameter, d_{va}, and (b) mass-mobility exponent, D_{fm}, prefactor, k_m, for 4 ml/min precursor flow rate at 0.5 M Zr concentration. A higher O_2 flow rate reduces the high temperature residence time and so decreases the d_{va}. The d_{va} obtained online during the DMA–APM measurement by Eq. (10) using k_a and D_α of aggregates (Fig. 2) is in good agreement with the average diameter obtained by nitrogen adsorption (BET) measurements (squares) and counting TEM for flame 4/5. The D_{fm} are independent of the O_2 flow rate varying from 3 to 7 l/min and are consistent with D_{fm} for cluster–cluster agglomerates [22] or aggregates at the beginning of sintering [12]. Normalizing the agglomerate/aggregate mobility diameter and mass with the average primary particle diameter and mass, respectively, collapses all measurements on a single line independent of O_2 flow rate.

D_α = 1.08) and aggregates (circles, solid black line, k_a = 1.0 and D_α = 1.07) averaged over each mobility size as a function of O_2 flow rate (please see Appendix A.4 for an example calculation). The error bars are ± one standard deviation of d_{va} from every d_m at a given O_2 flow rate. So, small error bars indicate that the primary particle size is independent of d_m or fractal-like particle size, consistent with TEM images (Fig. 5) and counts (Table 2). The $d_{va,B}$ measured by N_2 adsorption (squares) decreases from 14.7 nm at 3 l/min O_2 to 9.7 nm at 7 l/min O_2 flow rate (Fig. 7a). The d_{va} by DMA–APM with k_a and D_α for aggregates (circles) is in better agreement with $d_{va,B}$ than that for agglomerates for all O_2 flow rates. The $d_{va,T}$ from TEM (diamonds) for the 4/5 flame (Table 2) is also slightly closer to the d_{va} for aggregates rather than agglomerates indicating a limited degree of hard necking.

The present analysis (Eq. (10)) allows determining the surface area mean primary particle diameter, d_{va} (or SSA, Eq. (11)) and number, n_{va}, by DMA–APM measurements in addition to d_m, m and D_{fm}, k_{APM}. Furthermore, the agglomerate or aggregate surface

area a can be estimated by a simple transformation of Eq. (10): $a = 6v/d_{va}$. Fig. 7b shows the n_{va} as a function of d_m/d_{va} for the DMA–APM data of flames 4/3, 4/5, and 4/7 in a double logarithmic plot [8]. These data fall largely on a straight line for each flame leading to extraction of D_{fm} and k_m from Eqs. (2) and (3). These fractal-like particles have a $D_{fm} \approx 2.15$ and $k_m \approx 1$ consistent with cluster–cluster aggregates at their onset of sintering [[12]: Fig. 6] regardless of O_2 flow rate (Fig. 7b). This is similar to DMA–APM measurements of SiO_2 fractal-like particles generated in laminar diffusion flames [35]. There increasing O_2 flow rates had decreased D_{fm} [[35]: Fig. 9] approaching an asymptotic value.

The structure of FSP-made ZrO_2 particles here was affected rather little by increasing O_2 flow rate. These particles were slightly aggregated given that their PPs followed closer the power law (Eq. (1)) parameters (D_α, k_a) for aggregates rather than those for agglomerates (Fig. 7a). The PPs exhibited however rather limited degree of aggregation given that D_{fm} hardly changed from the value (2.15) of agglomerates. The turbulence of the FSP process leads to

Fig. 8. The effect of ZrO_2 precursor flow rate on (a) surface area mean primary particle diameter, d_{va}, and (b) mass-mobility exponent, D_{fm}, and prefactor, k_m, is investigated at 5 l/min O_2 flow rate and 0.5 M Zr concentration. Increasing precursor flow rate results in longer particle residence times at high temperature and thus larger primary particles. The d_{va} increases from ∼11 nm at 4 ml/min to ∼25 nm at 12 ml/min precursor flow rate. The d_{va} estimated online with Eq. (10) for aggregates are in good agreement with d_{va} from nitrogen adsorption measurements while counting TEM images gives d_{va} in-between the d_{va} from aggregates and agglomerates. A $D_{fm} \approx 2.15$–2.2 is an indication of diffusion-limited or ballistic cluster–cluster agglomerates [22] or aggregates at the beginning of sintering [12]. The DMA–APM data collapse on a single line if normalized by the primary particle diameter and mass, respectively, indicating that the structures are similar.

short particle residence times at high temperature so that varying the O_2 flow rate hardly affects the D_f (or D_{fm} here) of product particles in contrast to laminar diffusion flames [7].

4.3.2. Effect of precursor flow rate

The effect of precursor flow rate on average primary particle diameter, d_{va}, and particle morphology is investigated for 5 l/min O_2 flow rate at 0.5 M Zr (Fig. 8) by DMA–APM measurements. The fractal-like particle mass m was measured for mobility diameters d_m = 30–400 nm with precursor feed rates of 4, 8, and 12 ml/min corresponding to 14.8, 29.6, and 44.4 g/h production rates. These fractal-like particles are in the transition regime ($Kn = 2\lambda/d_m$ = 0.33–4.45) at room temperature.

Fig. 8a shows by *ex situ* BET (squares) and TEM (diamonds) measurements that larger primary particles are formed with increasing precursor flow rates consistent with literature [10]. Increasing precursor flow rate increases flame enthalpy, length, and particle concentration resulting in faster sintering and coagulation [42]. Using the k_a and D_α of sintering cluster–cluster aggregates (Fig. 2: circles), the d_{va} (Eq. (10)) are 11.3 ± 0.4, 16.7 ± 1.4, and 24.1 ± 4.1 nm (Table 1) in close agreement with the measured $d_{va,B}$ and $d_{va,T}$ (Fig. 5). The $d_{va,T}$ is slightly smaller than $d_{va,B}$, which is again an indication of necking between particles [10], consistent with TEM images (Fig. 5). Fig. 8a also shows the d_{va} for agglomerates (triangles, broken red line: k_a = 1.11 & D_α = 1.08). This d_{va} is not that far from that for aggregates (solid black line) indicating again a limited degree of aggregation between the primary particles.

For the data shown in Fig. 8b, the D_{fm} is 2.18 ± 0.03, 2.17 ± 0.05, and 2.06 ± 0.20 for precursor flow rates of 4, 8, and 12 ml/min, respectively. The error (inset) represents the regression error. This D_{fm} is again close to that of ballistic or diffusion-limited cluster–cluster agglomerates [22,34] or aggregates at the onset of sintering [[12]: Fig. 6a]. The precursor flow rate hardly affects D_{fm} for 4 or 8 though the error increases for 12 ml/min. The DMA–APM data collapse again onto one line with k_m close to 1 for agglomerates or weakly sintered aggregates (Fig. 8b). Similarly to the effect of O_2 flow rate (Fig. 7), the fractal-like ZrO_2 particles made at these

conditions (0.5 M of ZrEHA) had limited degree of aggregation given their $D_{fm} \sim 2.15$ and that the measured $d_{va,B}$ (squares) and $d_{va,T}$ (diamonds) were closer to the d_{va} for aggregates (solid black line) than agglomerates (broken red line).

4.3.3. Effect of zirconium concentration and precursor composition

Fig. 9a compares the d_{va} by DMA–APM for aggregates (circles) and agglomerates (triangles) and BET (squares) measurements as a function of molarity of ZrEH (filled symbols) and ZrEHA (open symbols). Table 1 shows that the ZrEH-made ZrO_2 particles generated at 0.05–0.5 M Zr correspond to 1.5–15 g/h production rate while the ZrEHA-made ones at 0.5–2 M Zr correspond to 15–60 g/h production rate at 5 l/min O_2 and 4 ml/min precursor feed rate (flame 4/5). The d_{va} increases from ∼5 nm at 0.05 M to ∼15 nm at 2 M Zr.

The $d_{va,B}$ by nitrogen adsorption at 0.5 M Zr is not affected by precursor composition (both open and filled squares overlap) and is within the error bar for the DMA–APM measurement for aggregates (Table 1). For Zr < 0.5 M, the agreement between BET measurements ($d_{va,B}$) and d_{va} (Eq. (10)) with k_a and D_α for agglomerates is slightly better than that of d_{va} for aggregates, indicating limited necking between particles. For the small particles made at low precursor concentrations, coalescence takes place rapidly upon collision. Agglomerates are formed only downstream at lower temperatures, where hardly any sintering takes place. This is similar to Mueller et al. [6] who found no fractal-like structures of SiO_2 powder compacts made in laminar flames at low production rates (9 g/h). For concentrations up to 0.5 M ZrEH, the $d_{va,B}$ (filled squares) follows also the relationship $d_{va} \propto V^{2/5}$ (dotted line) for coagulation and full coalescence of spherical particles in the free molecular regime [43], where V is the ZrO_2 volume concentration. Thus, the increase in d_{va} can be explained largely by coagulation and instantaneous coalescence at low Zr concentrations (<0.5 M Zr). The concentration of ZrO_2 in the flame increases with higher precursor molarity while the particle residence time at high temperatures stays almost constant, as it is mainly influenced by O_2 and precursor solution flow rates [44]. So, the primary particle
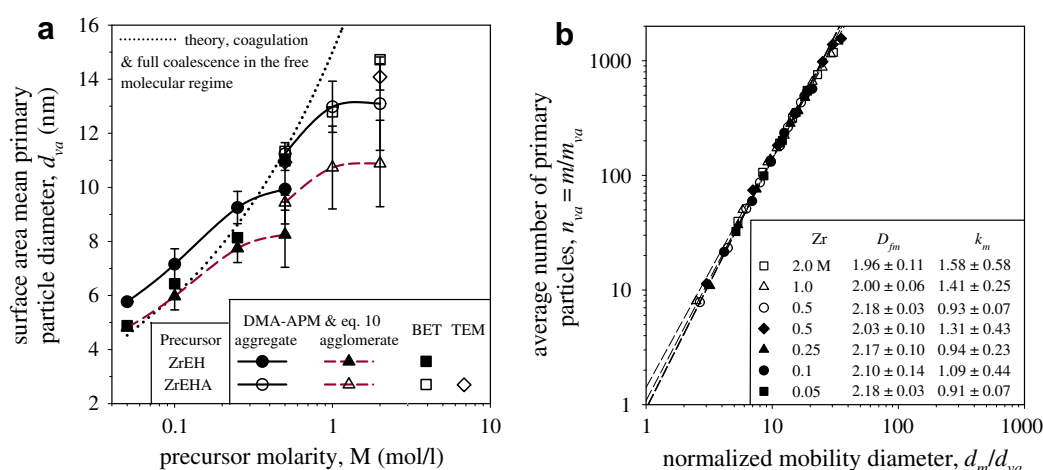
Fig. 9. The effect of Zr precursor concentration from 0.05 to 0.5 M for Zr–ethylhexanoate and from 0.5 to 2 M for Zr–2ethylhexanoic acid, both in xylene, on (a) surface area mean primary particle diameter, d_{va}, and (b) mass-mobility exponent, D_{fm}, and prefactor, k_m, of ZrO_2 particles made in flame 4/5 (4 ml/min precursor and 5 l/min O_2 flow rates). Increasing the Zr precursor concentration results in faster coagulation and larger d_{va}. The two different precursors result in the same d_{va} at 0.5 M Zr, indicating no effect of precursor composition on particle morphology. The d_{va} assuming agglomerates (Eq. (12), red broken line) is closer to that from N_2 adsorption (filled square, BET) measurements for Zr < 0.5 M. In contrast, the d_{va} assuming aggregates (Eq. (13), black solid line) is closer to BET (open squares) and TEM (open diamonds) measurements for Zr ⩾ 0.5 M. The growth of d_{va} of agglomerates closely follows the theory for coagulation and perfect coalescence (black dotted line) for Zr < 0.5 M. When aggregate or agglomerate mass, m, and mobility diameter, d_m, are normalized by the corresponding average primary particle mass and d_{va}, respectively, they collapse onto a single line, indicating that they follow a power law. The D_{fm} are independent of precursor concentration consistent with cluster–cluster made agglomerates [22] or aggregates at the beginning of their sintering [12]. So, the Zr concentration does not affect agglomerate structure at these conditions. (For interpretation of the references to color in this figure legend, the reader is referred to the web version of this article.)

diameter increases continuously by increasing particle concentration in the flame [45], a coagulation-limited particle growth.

At increased Zr concentration (0.5–2 M), the $d_{va,B}$ (open squares) is closer to that from aggregates (open circles) than from agglomerates (Fig. 9a): for ZrEHA 0.5 and 1 M, the $d_{va,B}$ (open squares) is right on the d_{va} for aggregates (open circles) while for 2 M, it is within the error bar of the latter. At 2 M, the $d_{va,T}$ (diamond) is also between d_{va} from DMA–APM and $d_{va,B}$ and $\sigma_{g,p} = 1.37$, which is identical to that at 0.5 M (4/5 flame in Table 2). A $\sigma_{g,p}$ smaller than that of the self-preserving size distribution (1.45) points to aggregate formation [36]. Furthermore, all measured surface area mean primary particle diameters, d_{va}, are below that predicted by theory (dotted line)[43] indicating that particle growth is no longer coagulation-controlled. This further supports the notion that at these high Zr concentrations, the degree of aggregation has increased. Again this is consistent with Mueller et al. [6] who found that SiO_2 particles made at high production rates (17 g/h) and O_2 flow rates (13.3–24 l/min) in laminar diffusion flames were fractal-like by SAXS.

Fig. 9b shows the mass-mobility relation of fractal-like ZrO_2 particles that have again a D_{fm} consistent with cluster–cluster made agglomerates [22] or aggregates at the onset of sintering [12]. The D_{fm} is essentially independent of precursor concentration. The prefactor k_m is around 1 and the DMA–APM data collapse practically onto one line indicating that the ZrO_2 agglomerates or aggregates are generated by cluster–cluster collisions and have increased extent of aggregation with increasing precursor concentration that leads to hotter flames and higher particle concentrations.

A mass-mobility exponent of $D_{fm} \approx 2.15$ is obtained for agglomerates and aggregates at the beginning of sintering formed by cluster–cluster coagulation with: (a) primary particles in the free molecular or transition regime and (b) a primary particle size distribution of $\sigma_g \leqslant 1.5$ [34]. For example, Ag, TiO$_2$, and Si agglomerates generated by evaporation/condensation [25,46–48], flame-generated soot, and Diesel exhaust [49], SiO$_2$ generated by a diffusion flame [35] or the present ZrO_2 agglomerates by flame spray pyrolysis have $D_{fm} \approx 2.15$. However, further sintering of these agglomerates results in more compact structures and higher D_{fm} as shown for silver [46] and silica aggregates [35] and by mesoscale simulations [12]. Furthermore, agglomerates that are coated with oil, water or other condensates, a common occurrence for soot in the atmosphere, restructure and have a larger D_{fm} than 2.15 [50]. Also, restructuring of agglomerates under shear results in $D_{fm} > 2.15$ [51].

5. Conclusions

A method to extract the average primary particle diameter of fractal-like nanostructured particles from nearly *in situ* mass-mobility measurements is presented. The primary particle diameter is a key characteristic of nanomaterials as it determines their unique or novel properties over those of bulk material. Till now, this property is largely determined by *ex situ* techniques, most notably by microscopy and nitrogen adsorption. The present method is elucidated with fractal-like ZrO_2 nanoparticles made by scalable flame spray pyrolysis and characterized by DMA–APM measurements and a power law. That way, the average primary particle number and surface area mean diameter of fractal-like ZrO_2 particles (agglomerates or aggregates) are obtained without requiring separate microscopic or nitrogen adsorption measurements or fitting to a subset of data. This mass-mobility determined primary particle diameter was in good agreement with primary particle diameters from counting TEM images and nitrogen adsorption measurements. In fact, the proximity of the DMA–APM primary particle diameter for aggregates to that determined by N$_2$

adsorption or TEM-image counting provided an indication to the extent of aggregation of these fractal-like particles.

The primary particle diameter varied between 5 and 25 nm and the mobility diameter from 30 to 400 nm depending on process conditions. These flame-made fractal-like particles rapidly obtain the self-preserving size distribution corresponding to their fractal dimension. Longer particle residence times at high temperatures and high precursor concentrations resulted in larger primary particles with increased degree of aggregation. The fractal-like zirconia particles have a mass-mobility exponent, $D_{fm} \approx 2.15$, and prefactor, $k_m \approx 1$, independent of investigated process conditions and corresponding primary particle diameter distributions. These values are consistent with fractal-like particles formed by cluster–cluster coagulation. In addition, increased particle concentration led progressively to more aggregated flame-made particles with increased primary particle polydispersity. At low particle concentrations, agglomerate particles were formed with little necking between primary particles.

Appendix A

A.1. Estimation of the peak of the APM mass distribution of multiply charged particles

The segregated particle mass by the APM is calculated with a force balance [16]:

$$m \cdot r_{avg}^2 \cdot \omega^2 = V_{APM} \cdot q/(\log(r_{out}/r_{in})) \tag{A1}$$

The mass to number of charges ratio is:

$$m_{APM} = \frac{m}{n_c} = \frac{V_{APM} \cdot e}{\left(r_{avg}^2 \cdot \omega^2 \cdot \log(r_{out}/r_{in})\right)} \tag{A2}$$

So, a doubly charged particle ($n_c = 2$) has a peak at half its mass in the APM. A simplified theory for the DMA results in a mobility to charge ratio of [52]:

$$\frac{d_m}{C(d_m) \cdot n_c} = \frac{2V_{DMA}L \cdot e}{3\eta Q \ln(r_2/r_1)}, \tag{A3}$$

where V_{DMA} is the DMA voltage, $L = 0.44369$ m is its length, Q is the sheath air flow rate, η is the gas viscosity and $r_2 = 0.01961$ m and $r_1 = 0.00937$ m are the outer and inner radii of the annular space, respectively, and C_c is the Cunningham correction factor. Singly charged particles ($n_c = 1$) with $d_m \approx 200$ nm are collected with $Q = 7$ l/min and $V_{DMA} = 3750$ V at 293 K and 1 atm in air. These particles have theoretically $m = 1.8724$ fg. The mass is calculated with Eq. (3) and assuming $d_p = d_{va} = 10$ nm, $D_{fm} = 2.15$ and $k_m = 1$ as observed in our experiments. Doubly charged particles ($n_c = 2$) also passing the DMA have $d_m \approx 325$ nm (solving Eq. (A3)) under the same conditions (V_{DMA} & Q) and a mass $m = 5.4897$ fg. The APM segregates particles according to Eq. (A1) and shows a peak at $m_{APM} = m/2 = 2.75$ fg.

A.2. Derivation of Eq. (10)

The projected areas of agglomerate/aggregate, a_a, and primary particle, a_p, in Eq. (1) are written as a function of mobility, d_m (Eq. (6)), and primary particle diameter, d_p, respectively:

$$n_p = k_a \left(\frac{a_a}{a_p} \right)^{D_\alpha} = k_a \left(\frac{d_m}{d_p} \right)^{2D_\alpha}. \tag{A4}$$

For agglomerates of monodisperse primary particles the surface area mean diameter, $d_{va} = 6v/a$, is equal to d_p and the average number of primary particles n_{va} to the actual n_p, where v and a are agglomerate/aggregate volume and surface area. Fig. 2 shows that for aggregates with necks formed by sintering, Eq. (1) holds if d_p is replaced by d_{va} and n_p by n_{va}:

$$n_{va} = k_a \left(\frac{d_m}{d_{va}} \right)^{2D_\alpha}, \tag{A5}$$

where n_{va} is a function of agglomerate/aggregate mass, m, material density ρ and d_{va}:

$$n_{va} = \frac{v}{\pi d_{va}^3/6} = \frac{m/\rho}{\pi d_{va}^3/6}. \tag{A6}$$

Combining Eqs. (A5) and (A6) results in:

$$\frac{m/\rho}{\pi d_{va}^3/6} = k_a \left(\frac{d_m}{d_{va}} \right)^{2D_\alpha}. \tag{A7}$$

So, the d_{va} is written in terms of d_m, m and ρ:

$$d_{va} = \left(\frac{\pi k_a \rho}{6m} (d_m)^{2D_\alpha} \right)^{1/(2D_\alpha - 3)}. \tag{A8}$$

A.3. Mobility diameter distribution as-measured by DMA

Fig. A1 shows the fractal-like particle mobility diameter, d_m, distribution of Fig. 6 as-measured by a DMA without multiple charge correction. The fractal-like particles are generated with 8 ml/min precursor (0.5 M Zr) solution and 5 l/min O_2 flow rate. The particles have a geometric mean mobility diameter, $d_{m,g}$ = 107.3 nm and geometric standard deviation, $\sigma_{m,g}$ = 1.56. Both, $d_{m,g}$ and $\sigma_{m,g}$, are ~2% smaller than accounting for the multiple charge correction (Fig. 6a). The total number concentration N is 1.56×10^6 #/cm^3 and is 17% higher than that of the corrected distribution in Fig. 6a.
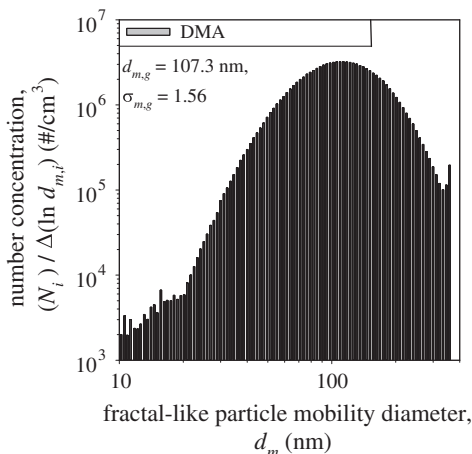
Fig. A1. The mobility diameter distribution of fractal-like particles generated with 8 ml/min precursor and 5 l/min O_2 flow rate at 0.5 M Zr concentration as-measured by a differential mobility analyser (DMA) without multiple charge correction.

A.4. Calculation of d_{va} from DMA–APM measurements

The DMA–APM measurements for the flame 4/5 (Fig. 4a) at 5 l/min O_2 flow and 4 ml/min precursor (0.5 M Zr) solution feed rate is chosen for demonstration. At a mobility diameter d_m = 110 nm and an APM rotation speed of 8000 rpm, the mode of the APM mass distribution is found at 250 V. In a first step, the mass is calculated with the force balance and the geometry of the APM [16]:

$$\begin{aligned} m &= \frac{V \cdot n_c \cdot e}{r_{avg}^2 \cdot \omega^2 \cdot \log(r_{out}/r_{in})} \\ &= \frac{250\,\text{V} \cdot 1 \cdot 1.6019e^{-19}\,\text{C}}{(0.051\,\text{m})^2 \cdot (8000 \cdot 2\pi/60\text{s})^2 \log(0.052/0.050)} = 0.5593\,\text{fg}, \end{aligned} \tag{A9}$$

assuming singly charged particles with n_c = 1 and the elementary charge $e = 1.6019e^{-19}$ C. The solid volume of the agglomerate is determined with the density of zirconia:

$$v = \frac{m}{\rho} = \frac{0.5593 \times 10^{-18}\,\text{kg}}{5720\,\text{kg/m}^3} = 9.778 \times 10^{-23}\,\text{m}^3 \tag{A10}$$

The d_{va} in an aggregate is obtained by Eq. (10) with D_α = 1.07 and k_a = 1.0:

$$\begin{aligned} d_{va} &= \left(\frac{\pi k_a}{6v} (d_m)^{2D_\alpha} \right)^{1/(2D_\alpha - 3)} \\ &= \left(\frac{\pi \cdot 1.0}{6 \cdot 9.778 \times 10^{-23}\,\text{m}^3} (1.1 \times 10^{-7}\,\text{m})^{2 \cdot 1.08} \right)^{1/(2 \cdot 1.08 - 3)} \\ &= 1.12 \times 10^{-8}\,\text{m} = 11.2\,\text{nm}. \end{aligned} \tag{A11}$$

This calculation is repeated for all measured mobility diameters, and the arithmetic mean d_{va} is obtained by averaging over all d_m. Finally, for each d_m, the average number of primary particles n_{va} is determined with d_{va}:

$$n_{va} = \frac{6v}{\pi d_{va}^3} = \frac{6 \cdot 9.778 \times 10^{-23}\,\text{m}^3}{\pi \cdot (1.12 \times 10^{-8}\,\text{m})^3} = 132.53 \approx 133. \tag{A12}$$

The ZrO_2 agglomerates with a mobility size of 110 nm have on average 133 primary particles of 11.2 nm (Table 1).

References

[1] P. Meakin, Adv. Colloid Interface Sci. 28 (1988) 249.
[2] J.H. Scheckman, P.H. McMurry, J. Aerosol Sci. 42 (2011) 508.
[3] A.D. Maynard, E.D. Kuempel, J. Nanopart. Res. 7 (2005) 587.
[4] C.M. Sorensen, J. Cai, N. Lu, Appl. Opt. 31 (1992) 6547.
[5] Y.C. Xing, U.O. Koylu, D.E. Rosner, Appl. Opt. 38 (1999) 2686.
[6] R. Mueller, H.K. Kammler, S.E. Pratsinis, A. Vital, G. Beaucage, P. Burtscher, Powder Technol. 140 (2004) 40.
[7] A. Camenzind, H. Schulz, A. Teleki, G. Beaucage, T. Narayanan, S.E. Pratsinis, Eur. J. Inorg. Chem. (2008) 911.
[8] K. Park, F. Cao, D.B. Kittelson, P.H. McMurry, Environ. Sci. Technol. 37 (2003) 577.
[9] J. Wang, W.G. Shin, M. Mertler, B. Sachweh, H. Fissan, D.Y.H. Pui, Aerosol Sci. Technol. 44 (2010) 97.
[10] R. Mueller, R. Jossen, H.K. Kammler, S.E. Pratsinis, AIChE J. 50 (2004) 3085.
[11] R. Mueller, R. Jossen, S.E. Pratsinis, M. Watson, M.K. Akhtar, J. Am. Ceram. Soc. 87 (2004) 197.
[12] M.L. Eggersdorfer, D. Kadau, H.J. Herrmann, S.E. Pratsinis, J. Aerosol Sci. 46 (2012) 7.
[13] L. Madler, H.K. Kammler, R. Mueller, S.E. Pratsinis, J. Aerosol Sci. 33 (2002) 369.
[14] A.J. Grohn, S.E. Pratsinis, K. Wegner, Chem. Eng. J. 191 (2012) 491.
[15] T. Johannessen, S.E. Pratsinis, H. Livbjerg, Powder Technol. 118 (2001) 242.
[16] K. Ehara, C. Hagwood, K.J. Coakley, J. Aerosol Sci. 27 (1996) 217.
[17] E.D. Whitney, Ceramic Cutting Tools: Materials, Development and Performance, William Andrew Publishing, New Jersey, 1994.
[18] M.D. Abramoff, P.J. Magalhaes, S.J. Ram, Biophoton. Int. 11 (2004) 36.
[19] A.I. Medalia, J. Colloid Interface Sci. 24 (1967) 393.
[20] P. Meakin, B. Donn, G.W. Mulholland, Langmuir 5 (1989) 510.
[21] C.M. Megaridis, R.A. Dobbins, Combust. Sci. Technol. 71 (1990) 95.
[22] C.M. Sorensen, Aerosol Sci. Technol. 45 (2011) 755.
[23] J. Cai, C.M. Sorensen, Phys. Rev. E 50 (1994) 3397.
[24] P. Chan, B. Dahneke, J. Appl. Phys. 52 (1981) 3106.
[25] S.N. Rogak, R.C. Flagan, H.V. Nguyen, Aerosol Sci. Technol. 18 (1993) 25.

[26] K. Park, D.B. Kittelson, P.H. McMurry, Aerosol Sci. Technol. 38 (2004) 881.
[27] S.N. Rogak, R.C. Flagan, Part. Part. Syst. Char. 9 (1992) 19.
[28] A.A. Lall, S.K. Friedlander, J. Aerosol Sci. 37 (2006) 260.
[29] B. Dahneke, Aerosol Sci. Technol. 1 (1982) 179.
[30] S.K. Friedlander, Smoke, Dust, and Haze: Fundamentals of Aerosol Dynamics, second ed., Oxford University Press, New York, 2000.
[31] R. Jullien, M. Kolb, R. Botet, J. Phys. Lett. 45 (1984) L211.
[32] M.L. Eggersdorfer, D. Kadau, H.J. Herrmann, S.E. Pratsinis, Langmuir 27 (2011) 6358.
[33] F. Pierce, C.M. Sorensen, A. Chakrabarti, Phys. Rev. E 74 (2006) 021411.
[34] M.L. Eggersdorfer, S.E. Pratsinis, Aerosol Sci. Technol. 46 (2012) 347.
[35] J.H. Scheckman, P.H. McMurry, S.E. Pratsinis, Langmuir 25 (2009) 8248.
[36] M.C. Heine, S.E. Pratsinis, J. Aerosol Sci. 38 (2007) 17.
[37] S. Vemury, S.E. Pratsinis, J. Aerosol Sci. 26 (1995) 175.
[38] A. Wiedensohler, J. Aerosol Sci. 19 (1988) 387.
[39] S. Tsantilis, H.K. Kammler, S.E. Pratsinis, Chem. Eng. Sci. 57 (2002) 2139.
[40] W.C. Hinds, Aerosol Technology: Properties, Behavior, and Measurement of Airborne Particles, John Wiley & Sons, New York, 1999.
[41] S. Vemury, K.A. Kusters, S.E. Pratsinis, J. Colloid Interface Sci. 165 (1994) 53.
[42] S.E. Pratsinis, W.H. Zhu, S. Vemury, Powder Technol. 86 (1996) 87.
[43] W. Koch, S.K. Friedlander, Part. Part. Syst. Char. 8 (1991) 86.
[44] R. Mueller, L. Madler, S.E. Pratsinis, Chem. Eng. Sci. 58 (2003) 1969.
[45] K. Wegner, S.E. Pratsinis, AIChE J. 49 (2003) 1667.
[46] S.C. Kim, J. Wang, M.S. Emery, W.G. Shin, G.W. Mulholland, D.Y.H. Pui, Aerosol Sci. Technol. 43 (2009) 344.
[47] A. Schmidt-Ott, J. Aerosol Sci. 19 (1988) 553.
[48] W.G. Shin, G.W. Mulholland, S.C. Kim, J. Wang, M.S. Emery, D.Y.H. Pui, J. Aerosol Sci. 40 (2009) 573.
[49] M.M. Maricq, X. Ning, J. Aerosol. Sci. 35 (2004) 1251.
[50] R. Zhang, A.F. Khalizov, J. Pagels, D. Zhang, H. Xue, P.H. McMurry, PNAS 105 (2008) 10291.
[51] M.L. Eggersdorfer, D. Kadau, H.J. Herrmann, S.E. Pratsinis, J. Colloid Interface Sci. 342 (2010) 261.
[52] E.O. Knutson, K.T. Whitby, J. Aerosol Sci. 6 (1975) 443.